IOP Publishing New J. Phys. 26 (2024) 023035 https://doi.org/10.1088/1367-2630/ad26bb

New Journal of Physics
The open access journal at the forefront of physics

Deutsche Physikalische Gesellschaft DPG
IOP Institute of Physics
Published in partnership with: Deutsche Physikalische Gesellschaft and the Institute of Physics

OPEN ACCESS

RECEIVED
29 May 2023

REVISED
30 January 2024

ACCEPTED FOR PUBLICATION
6 February 2024

PUBLISHED
19 February 2024

PAPER

The suppression of finite size effect within a few lattice sites

Tao Liu[1], Kai Bai[1], Yicheng Zhang[1], Duanduan Wan[1,*], Yun Lai[2], C T Chan[3] and Meng Xiao[1,4,*]

[1] Key Laboratory of Artificial Micro- and Nano-structures of Ministry of Education and School of Physics and Technology, Wuhan University, Wuhan 430072, People's Republic of China
[2] National Laboratory of Solid State Microstructures, School of Physics, and Collaborative Innovation Center of Advanced Microstructures, Nanjing University, Nanjing 210093, People's Republic of China
[3] Department of Physics, The Hong Kong University of Science and Technology, Clear Water Bay, Kowloon, Hong Kong Special Administrative Region of China 999077, People's Republic of China
[4] Wuhan Institute of Quantum Technology, Wuhan 430206, People's Republic of China
* Authors to whom any correspondence should be addressed.

E-mail: ddwan@whu.edu.cn and phmxiao@whu.edu.cn

Keywords: topological boundary modes, finite size effect, crosstalk, plasmonic spheres

Abstract

Boundary modes localized on the boundaries of a finite-size lattice experience a finite size effect (FSE) that could result in unwanted couplings, crosstalks and formation of gaps even in topological boundary modes. It is commonly believed that the FSE decays exponentially with the size of the system and thus requires many lattice sites before eventually becoming negligibly small. Here we consider a two-dimensional strip geometry that is periodic along one direction and truncated along the other direction, in which we identify a special type of FSE of some boundary modes that apparently vanishes at some particular wave vectors along the periodic direction. Meanwhile, the number of wave vectors where the FSE vanishes equals the number of lattice sites across the strip. We analytically prove this type of FSE in a simple model and prove this peculiar feature. We also provide a physical system consisting of a plasmonic sphere array where this FSE is present. Our work points to the possibility of almost arbitrarily tunning of the FSE, which facilitates unprecedented manipulation of the coupling strength between modes or channels such as the integration of multiple waveguides and photonic non-abelian braiding.

1. Introduction

A bound state can be trapped by a barrier. When the width and height of this barrier are not infinitely large, there is some probability that the state can tunnel through this barrier. These size-dependent phenomena are commonly called the finite size effect (FSE). FSE is ubiquitous for both quantum and classical waves. The barrier here can be a potential barrier such as a quantum dot [1, 2] or originates from a band gap material [3, 4]. Besides the intrinsic absorption loss, the probability of tunneling determines the lifetime of these trapped states, which is crucial for quantum information processing [5–8]. Control over the tunneling probability also enables manipulating interaction between different trapped states to generate various entangled quantum states [9–11]. Meanwhile, fine-tuning of the coupling coefficient is a key requirement in programmable photonic simulators [12], non-abelian braiding of photons [13] and quantum computers [14], especially when nanostructure are considered.

Similar to trapped states, propagating states such as the waveguide modes also exhibit FSE [15]. The tails of waveguide modes extend outside the waveguide with a length scale characterized by the penetration depth. If two waveguides are placed within the penetration depth of each other, there will be unavoidable intercoupling. The crosstalk between waveguides limits the integration of multiple waveguide channels into a compact device [16]. Boundary (hinge) modes localized on the boundaries of a strip (hinge of a bar) geometry of a periodic lattice can also be regarded as waveguide modes. With the recent explosive growth of research in topological physics [17–20], topological boundary modes and hinge modes associated with nontrivial bulk topologies have attracted a lot of attention due to their robustness against disorder and fabrication imperfections [21–26]. However, these boundary and hinge modes also suffer from the FSE when the width of the system is not large enough [27–30]. So, even topological edge modes can be gapped if the width is not big enough to stop the coupling of modes localized on the opposite edges of the sample. On the other hand, controlling the FSE of topological boundary modes or hinge modes can achieve new versatile controllability, such as spin flipping [31], electrical switching [32], *etc.*

In this paper, we present a novel type of FSE of boundary modes. Without loss of generality, we consider the boundary modes on a two-dimensional (2D) strip geometry which is periodic along one direction and truncated along the other direction. Thus, there are two boundaries for such a 2D strip geometry. The boundary modes localized on opposite sides (if they exist) interact with each other, giving rise to an FSE-induced gap. Different from the prevailing understanding that the FSE vanishes only when the width of the strip is large enough, we discovered that the FSE could vanish at specific wave vectors (nodes) along the periodic direction in a narrow finite-width strip. Interestingly, the number of nodes equals the number of lattice sites perpendicular to the boundary, i.e. the width of the strip. Using a model Hamiltonian, we analytically solved this system and proved the existence of this novel feature, and then demonstrated a filtering effect by utilizing this unique feature. Such a peculiar FSE is a pure single-particle effect without the correlation among particles. Our system consists of only in-plane dipole orbitals and hence should represent general physics. Moreover, we provide a physical system composed of a plasmonic sphere array where this peculiar FSE can be observed. Our work demonstrates the possibility of completely suppress the FSE within a few lattice sites. This unique property can facilitate the manipulation of the coupling strength between modes or channels which are required in scenarios such as photonic non-abelian braiding [13] and integrating multiple waveguides [16].

The remainder of this paper is organized as follows. In section 2, we compare the difference between the typical FSEs and this special type of FSE considered in our work. We provide a tight-binding model Hamiltonian based on coupled in-plane dipoles P_x and P_y. The FSE vanishes at some specific wavevectors (denoted as nodes). We show that the number of nodes equals the number of lattice sites along the y-direction (N_y). In section 3, we present the filtering effect by using this unique FSE to filter out the component we need. In section 4, we show that this peculiar type of FSE also exists in a plasmonic sphere array whereat the coupling is not limited to nearest neighbors. Finally, we summarize in section 5.

2. Models of the peculiar type of FSE

Our system is shown in figure 1(a) which is periodic along the x-direction and finite along the y-direction. Each unit cell contains one atom or meta-atom which can support multiple modes such as S, P_x, P_y, P_z, *etc.* These modes interact and evolve into bands in momentum space and the physics can be captured succinctly using the usual tight-binding description. Inside a band gap, the system may exhibit boundary modes if the parameters are appropriately chosen, as shown schematically in figure 1(a) with the red and blue shaded regions denoting the mode profiles. These boundary modes can either be Shockley states [33], Tamm states [34] or originate from topological reasons [17, 18, 20, 21]. In figure 1(b), we sketch the typical consequences of the FSE for a strip geometry of the system. Here the shaded areas represent the projection of bulk bands, and the blue and red lines represent the dispersion of the boundary modes. We can use a two-level system to illustrate the interaction between the two boundary modes of a strip geometry. We start with the case when the strip is wide enough, there we can find two degenerate boundary modes (denoted as $|\varphi_1\rangle$ and $|\varphi_2\rangle$) localized on both sides of the strip. When the width of the strip is finite, FSE introduces perturbations on the system. Since there are no other modes inside the bandgap, any eigenmodes with frequency inside the gap of a finite system can be approximated by a linear combination of $|\varphi_1\rangle$ and $|\varphi_2\rangle$. In other words, with $|\varphi_1\rangle$ and $|\varphi_2\rangle$ as the basis, any eigenmode can be written as a normalized vector $|\psi\rangle = (c_1, c_2)^T$, where c_1 and c_2 are complex numbers. Let ε_0 represent the energy of $|\varphi_1\rangle$ and $|\varphi_2\rangle$, and κ denote the interaction of $|\varphi_1\rangle$ and $|\varphi_2\rangle$ introduced by the perturbations. When the strip is wide enough, the boundary modes on opposite sides of the strip decouple ($\kappa = 0$) and thus should exhibit the same dispersion if the system possesses mirror symmetry (m_y) as in our case. For a strip geometry with a finite width, two boundary modes interact with each other ($\kappa \neq 0$). If one focuses on the modes inside the bandgap, then the system can be approximated by an effective Hamiltonian:

$$H = \begin{pmatrix} \varepsilon_0 & \kappa \\ \kappa & \varepsilon_0 \end{pmatrix} \tag{1}$$

The eigenvalues and eigenvectors of a finite system are $\varepsilon_0 \pm \kappa$ and $\frac{1}{\sqrt{2}}(1, \pm 1)^T$, respectively. Here the sign $\pm$ correspond to the even/odd eigenmodes with respect to the mirror plane. In addition, the interaction due to the FSE on boundary modes introduces an energy splitting (a mini-gap with size 2κ). In other words, the presence of a min-gap as shown in figure 1(b) seems unavoidable. The strength of FSE herein can be easily calibrated as a function of k_x by inspecting the energy splitting between the even and odd boundary modes.

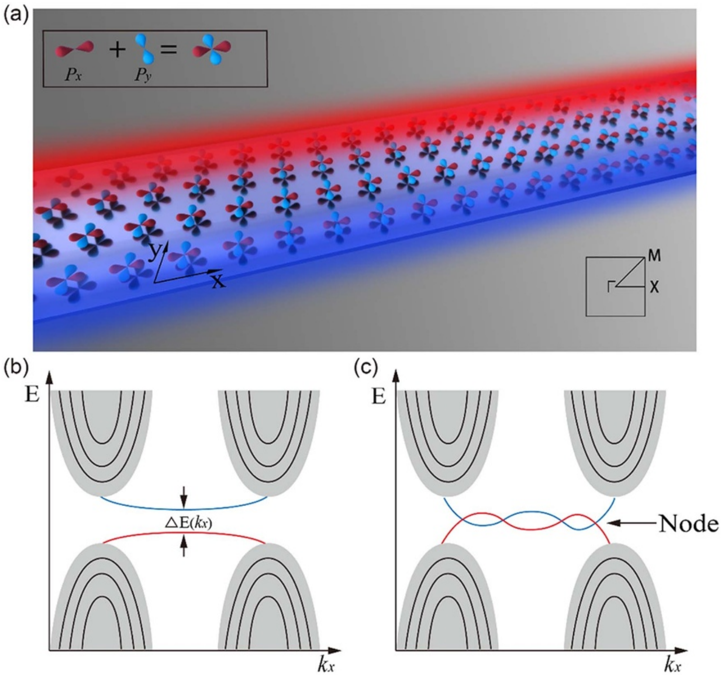

Figure 1. A peculiar type of FSE. (a) The coupling of two boundary modes (denoted by the red and blue shaded regions) localized on opposite sides of a strip geometry of a square lattice with P_x and P_y orbitals. The lower right inset shows the reciprocal space. (b)–(c) The schematic of two different types of FSEs, where the FSE is finite for all k_xs in (b) and vanishes at several nodes for certain k_xs in (c). The blue and red lines represent the dispersions of the two boundary modes of a strip geometry, and the gray regions together with the black lines denote the bulk bands.

In contrast to figure 1(b), we present here a special type of FSE as pictorially shown in figure 1(c). Due to the mirror symmetry, the boundary modes can couple to form even and odd modes, as shown respectively by the red and blue lines. They twist with each other and form several nodal points. As will be shown later, the FSE of the boundary modes vanishes at these nodal points (no interaction between boundary modes). Intriguingly, we find that the number of nodes equals the number of lattice sites along the y-direction (N_y). As long as the width of the strip is limited, the typical FSE shown in figure 1(b) always exists independent of wave vector. Distinctively, the peculiar FSE shown in figure 1(c) exhibits a unique feature in the sense that the FSE vanishes completely at some special wave vectors even though the width of the strip contains only a few lattice sites. Anomalous FSEs has been noted for helical boundary modes in topological insulator where the strength of the FSE decrease non-monotonically with the size [29, 30, 35], therein the oscillation length is hundreds or thousands of lattice constant. Therefore, the anomalous FSE is significantly different from our case as the FSE here oscillates at the lattice scale. Meanwhile, the two boundary modes in our case are related by mirror symmetry and thus exhibit the same dispersion in the absence of FSE. In contrast, the helical boundary modes in [27, 29, 30] exhibit opposite group velocities.

First, we take a 2D SSH model [36] as an example to show that typical boundary states show similar features as sketched in figure 1(b). As shown in figure 2(a), the real-space lattice structure of 2D SSH model is a square lattice, where each unit cell contains four sub-lattices. The physics is captured by nearest-neighbor hopping, and the real-space Hamiltonian can be written as

$$H = \sum\nolimits_{i,j} \left(t + \delta t x_{i,j}\right) c^{\dagger}_{i+1,j} c_{i,j} + \sum\nolimits_{i,j} \left(t + \delta t y_{i,j}\right) c^{\dagger}_{i,j+1} c_{i,j} + h.c. \tag{2}$$

where (i, j) denotes a lattice point in the square lattice, $c^{\dagger}$ and c are the creation and annihilation operators at the site (i, j), and t denotes the homogeneous background hopping strengths, δt is the alternating modulation term applying the background coupling strengths with $x_{i,j} = (-1)^i$ and $y_{i,j} = (-1)^j$, and '$h.c.$' stands for Hermitian conjugate. The intracell hopping (w) and intercell hopping (v), depicted as black and red lines respectively in figure 2(a), are defined as $w = t - \delta t$ and $v = t + \delta t$. Applying Fourier transformation in equation (2), the tight-binding Hamiltonian in momentum space can be obtained:

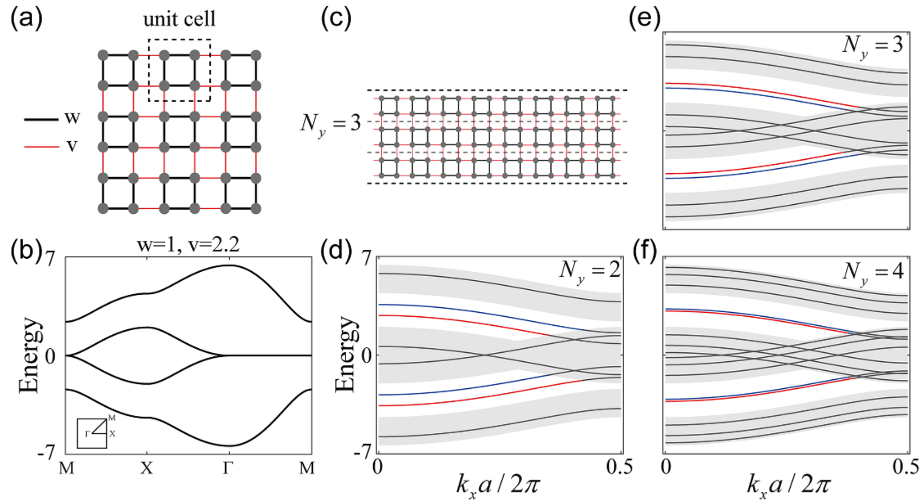

Figure 2. A typical consequence of the FSE in the 2D SSH model. (a) Schematic of 2D SSH model on a square lattice with only the nearest neighbor hopping. (b) The band structure of the periodic system with intracell hopping $w = 1$ and intercell hopping $v = 2.2$. The inset illustrates the reciprocal space of a square lattice, highlighting the high-symmetry points: Γ at the center of the Brillouin zone, X at the midpoint of the zone's edge, and M at the corner of the zone. (c) A sketch of a strip geometry of the 2D SSH model. The strip has N_y lattice sites along the y direction, and $N_y = 3$ is shown here. (d)–(f) The band structures for different N_ys, where the gray areas represent the projection of bulk bands, and the red (blue) curves are even (odd) modes with energy predominantly localized at the boundaries.

$$H = \begin{pmatrix} 0 & w + v\exp\left(ik_x\right) & 0 & w + v\exp\left(ik_y\right) \\ w + v\exp\left(-ik_x\right) & 0 & w + v\exp\left(ik_y\right) & 0 \\ 0 & w + v\exp\left(-ik_y\right) & 0 & w + v\exp\left(-ik_x\right) \\ w + v\exp\left(-ik_y\right) & 0 & w + v\exp\left(ik_x\right) & 0 \end{pmatrix}. \tag{3}$$

The topological phase transition for this system can be characterized by the bulk polarization $\boldsymbol{P} = \frac{1}{(2\pi)^2}\iint_{BZ} dk_x dk_y Tr\left[\boldsymbol{A}\left(k_x, k_y\right)\right]$, where $\boldsymbol{A}\left(k_x, k_y\right) = \langle u|i\nabla_{\boldsymbol{k}}|u\rangle$ is the Berry connection, $|u\rangle$ is the periodic part of Bloch function, the trace ('Tr') is taken over all the occupied bands, and the integration is over the first Brillouin Zone. Such a 2D SSH model exhibits the C_{4v} symmetry, whose point group is generated by two symmetry elements, a four-fold rotational axis (C_4) and a vertical mirror plane (σ_v). The C_4 symmetry signifies that the system keeps invariant under a rotation of $\pi/2$ around the z axis. This symmetry implies that the physical properties along the x and y directions are the same, thereby ensuring that $P_x = P_y$. Alternatively, the 2D Zak phase denoted with (θ_x, θ_y), can be determined by integrating the Berry connection along a specific direction, namely the k_x or k_y direction. The 2D Zak phase is defined as $\theta_{x(y)}\left(k_{y(x)}\right) = \frac{1}{2\pi}\int_{k_{y(x)}} dk_{x(y)} Tr\left[\boldsymbol{A}\left(k_x, k_y\right)\right]$, and it remains consistent for each corresponding value of $k_{y(x)}$ in this model. This characteristic is directly linked to the bulk polarization, where the relations $\theta_x = 2\pi P_x$ and $\theta_y = 2\pi P_y$ illustrate the connection between the Zak phase and the polarization components. The bulk polarization, as well as the Zak phase, determines the existence of topological boundary modes [37]. For instance, the nontrivial Zak phase $\theta_y = \pi$ results in the boundary modes along the x direction [36]. The topological phase transition point is at $w = v$. When $w = v$, all four bands are degenerate at the M point, and the middle two bands are also degenerate along the ΓM direction. When $w \neq v$, the first and fourth bands are gapped from the other bands, and the middle two bands remain degenerate along the ΓM direction. When $w > v$, the system is topologically trivial and characterized by a 2D Zak phase $(0, 0)$. Thus, there is no surface state when the system is truncated. On the other hand, when $w < v$, the parity sign of eigenstates at the X point changes after the band inversion at $w = v$ [36]. The system is topologically nontrivial and associated with a 2D Zak phase (π, π). Thus, surface states exist in the nontrivial phase when the system is truncated. Figure 2(b) shows the band structure of a nontrivial system with hopping strength $(w, v) = (1, 2.2)$ along the high symmetric directions in the Brillouin zone. There are two complete band gaps above the first band and below the fourth band. Hence, if the system is truncated, there are boundary modes located inside these two topological nontrivial band gaps.

Figure 2(c) sketches a strip geometry of the 2D SSH lattice which is periodic along the x-direction and finite along the y-direction. We denote the number of unit cells along the y-direction as N_y ($N_y = 3$ in figure 2(c)). Since this system exhibits mirror symmetry with respect to the y direction, there are two boundary modes localized on the upper and lower boundaries. The band structures for different N_y are shown in figures 2(d)–(f). Here, the light gray background represents the projection of the bulk periodic band. We focus on the $k_x > 0$ region as the $k_x < 0$ region is simply related by time-reversal symmetry. We start with $N_y = 2$, there are eight bands in total. Two boundary modes reside in the upper gap, and another two are located in the lower gap. Due to the FSE, the two boundary modes inside the same band gap coupled and split into one even mode and another odd mode as denoted by the red and blue lines, respectively. As N_y increases to 3 and 4, the two adjacent boundary mode dispersions get closer gradually as the coupling of the two boundary modes decreases. Similar to figure 1(b), there is no crossing between the boundary mode dispersions. Or in other words, there is always coupling between the boundary modes for an arbitrary k_x on the opposite sides of the strip.

Next, we provide a tight-binding model Hamiltonian that exhibits the salient features outlined in figure 1(c). This Hamiltonian is formulated to describe a dielectric particle array. The scattering and absorption of light for an array of dielectric particles exhibiting dipole resonances can be captured by the coupled-dipole approximation [38]. Thus, we derive this Hamiltonian with the coupled dipole equation [39]. We assume each site supports two dipoles P_x and P_y. For simplicity, we assume that other excitations are either far away in energy or are orthogonal to P_x and P_y (e.g. the P_z dipole). The ambient space is a vacuum, so no interactions are introduced other than the in-plane dipole interaction. The electric field generated by a dipole $\boldsymbol{P}_j$ is

$$E(r) = \frac{1}{4\pi\varepsilon_0}\left\{k^2\left(\boldsymbol{r}\times\boldsymbol{P}_j\right)\times\boldsymbol{r}\frac{e^{ikr}}{r^3} + \left[3\left(\boldsymbol{P}_j\cdot\boldsymbol{r}\right)\boldsymbol{r} - r^2\boldsymbol{P}_j\right]\left(\frac{1}{r^5} - \frac{ik}{r^4}\right)e^{ikr}\right\}, \tag{4}$$

where $\boldsymbol{r}$ is the displacement vector from the source dipole $\boldsymbol{P}_j$ to the observation point, and $k = \omega/c$ is the wave vector with ω and c being respectively, the frequency of the dipole and the speed of light in vacuum. When the wavelength $\lambda = 2\pi/k$ is much larger than the typical length scale of the system (e.g. the lattice constant a considered latter), we can take the quasi-static approximation and consider the dominate terms when $k \to 0$ [40]. Under this approximation, equation (4) is simplified to

$$E(r) = \frac{1}{4\pi\varepsilon_0}\frac{3\left(\boldsymbol{P}_j\cdot\boldsymbol{r}\right)\boldsymbol{r} - r^2\boldsymbol{P}_j}{r^5} = \frac{1}{4\pi\varepsilon_0}\overleftrightarrow{\boldsymbol{G}}(\boldsymbol{r})\cdot\boldsymbol{P}_j. \tag{5}$$

with the quasi-static Green tensor

$$\overleftrightarrow{\boldsymbol{G}}(\boldsymbol{r}) = \frac{3\boldsymbol{r}\otimes\boldsymbol{r} - r^2\overleftrightarrow{I}}{r^5}, \tag{6}$$

where the $\overleftrightarrow{I}$ is identity matrix. The induced dipole moment of the particle located at $\boldsymbol{R_i}$ is determined by the cumulative electric field generated by dipoles at all other lattice sites, the dipole moment $\boldsymbol{P_i}$ satisfy the coupled dipole equation:

$$\begin{aligned}\boldsymbol{P_i} &= \alpha(\omega)\sum\nolimits_{\boldsymbol{R}_j\neq\boldsymbol{R}_i}\boldsymbol{E}_{\boldsymbol{P}_j}(\boldsymbol{R}_i)\\ &= \alpha(\omega)\sum_{\boldsymbol{R}_j\neq\boldsymbol{R}_i}\frac{1}{4\pi\varepsilon_0}\overleftrightarrow{\boldsymbol{G}}\left(\boldsymbol{R}_i - \boldsymbol{R}_j\right)\cdot\boldsymbol{P}_j\\ &= \tilde{\alpha}(\omega)\sum_{\boldsymbol{R}_j\neq\boldsymbol{R}_i}\overleftrightarrow{\boldsymbol{G}}\left(\boldsymbol{R}_i - \boldsymbol{R}_j\right)\cdot\boldsymbol{P}_j,\end{aligned} \tag{7}$$

where $\boldsymbol{E}_{\boldsymbol{P}_j}(\boldsymbol{R}_i)$ denotes the electric field at $\boldsymbol{R}_i$ generated by the dipole $\boldsymbol{P}_j$ located at $\boldsymbol{R}_j$, $\alpha(\omega)$ is the polarizability of the particles, and $\tilde{\alpha}(\omega) = \frac{\alpha(\omega)}{4\pi\varepsilon_0}$. Thus, the coupled dipole equation can be reformulated as $\sum_{\boldsymbol{R}_j\neq\boldsymbol{R}_i}\overleftrightarrow{\boldsymbol{G}}\left(\boldsymbol{R}_i - \boldsymbol{R}_j\right)\cdot\boldsymbol{P}_j = \tilde{\alpha}^{-1}(\omega)\boldsymbol{P_i}$, which is similar as a Hermitian eigenvalue equation:

$$\boldsymbol{HP} = \epsilon(\omega)\boldsymbol{P} \tag{8}$$

where $\boldsymbol{P} = \left\{\ldots,\boldsymbol{P}_i,\ldots\boldsymbol{P}_j,\ldots\right\}$ denotes the dipole vector for real space, $\epsilon(\omega) = t\tilde{\alpha}^{-1}(\omega)$ denotes the energy of the system, and the Hermitian matrix nondiagonal element $H_{\boldsymbol{i},\boldsymbol{j}} = t\overleftrightarrow{\boldsymbol{G}}\left(\boldsymbol{R}_i - \boldsymbol{R}_j\right)$ denotes the hopping from a dipole $\boldsymbol{P}_j$ located at $\boldsymbol{R}_j$ to the dipole $\boldsymbol{P}_i$ at $\boldsymbol{R}_i$, the Hermitian matrix diagonal element is set as $H_{\boldsymbol{i},\boldsymbol{j}} = 0$. Here t is introduced only to ensure that the unit of hopping is energy [41]. The hopping strength $\overleftrightarrow{G}(r)$ between two dipoles decays cubically as a function of the inter-dipole distance r. The Hamiltonian containing all possible long-range hopping between two arbitrary dipoles includes an infinite series and is complicated to analyze. To obtain a simple tight-binding model, we truncate the hopping to the next nearest neighbor which are the minimal interactions needed to explain the physics presented in figure 1(c). The real-space lattice structure

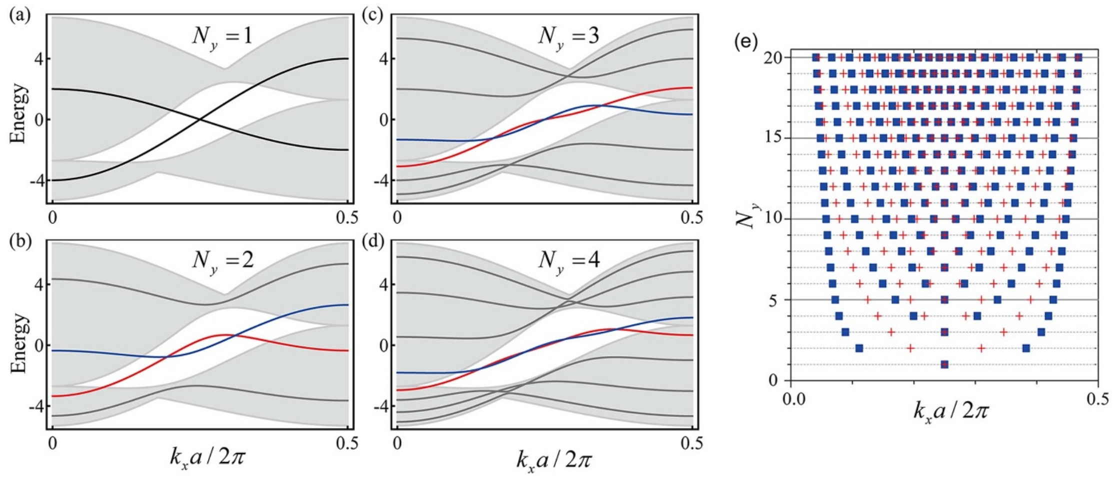

Figure 3. Band structure of the minimal model. (a)–(d) The band structures for different N_ys, where the gray areas represent the projection of bulk bands, and the red (blue) curves are even (odd) modes with energy predominantly localized at the boundaries. (e) The locations of nodes on the boundary modes (red plus signs) and the zeros of ΔE (blue square symbols, defined in equation (16)) for different N_ys.

of our model is a square lattice with each unit cell comprising a single atom that possesses in-plane dipole P_x and P_y, as shown in figure 1(a). We define the creation and annihilation operators $c^{\dagger}_{\boldsymbol{R}_i,px}, c_{\boldsymbol{R}_i,px}, c^{\dagger}_{\boldsymbol{R}_i,py}$ and $c_{\boldsymbol{R}_i,py}$ at the site $\boldsymbol{R}_i$, and the real-space Hamiltonian for a periodic system exhibiting the symmetry of C_{4v} point group can be written as

$$H=\sum\nolimits_{\boldsymbol{R}_i,\boldsymbol{R}_j\epsilon NN} t\left(-\boldsymbol{P}^{\dagger}_{\boldsymbol{R}_i}\overleftrightarrow{\boldsymbol{G}}\left(\boldsymbol{R}_i-\boldsymbol{R}_j\right)\boldsymbol{P}_{\boldsymbol{R}_j}\right)+\sum\nolimits_{\boldsymbol{R}_i,\boldsymbol{R}_j\epsilon NNN} t\left(-\boldsymbol{P}^{\dagger}_{\boldsymbol{R}_i}\overleftrightarrow{\boldsymbol{G}}\left(\boldsymbol{R}_i-\boldsymbol{R}_j\right)\boldsymbol{P}_{\boldsymbol{R}_j}\right) \tag{9}$$

where $\boldsymbol{P}_{\boldsymbol{R}_i}=\left(c_{\boldsymbol{R}_i,px}, c_{\boldsymbol{R}_i,py}\right)$ is the dipole operator's vector. The summation Σ_{NN} and Σ_{NNN} are over all nearest neighbor and next nearest neighbor hopping, respectively. Applying Fourier transformation, the momentum space Hamiltonian can be obtained:

$$H=\begin{pmatrix} -4\cos k_x+\cos k_y\left(2-\cos k_x/\sqrt{2}\right) & 3\sin k_x\sin k_y/\sqrt{2} \\ 3\sin k_x\sin k_y/\sqrt{2} & 2\cos k_x-\cos k_y\left(4+\cos k_x/\sqrt{2}\right) \end{pmatrix}. \tag{10}$$

Due to the C_{4v} symmetry, bands are degenerate at Γ and M. The bands are nondegenerate except for those two high symmetry points (see appendix A). We note that though we derive the Hamiltonian with the coupled dipole equation, a similar tight-binding Hamiltonian can also describe electronic systems of the same symmetry if p-orbitals (P_x and P_y) are dominant in the energy range of interest.

As we are interested in a strip geometry which is periodic along the x-direction and finite along the y-direction, we provide the projected band structure of the periodic system along the k_x direction as shown in figures 3(a)–(d) with the light gray background (the projected bulk band continuum) as a reference. Here we can focus on the $k_x>0$ region as the $k_x<0$ region is simply related by time-reversal symmetry. Now we have a band gap region between the two bands and the band gap closes only at $k_x=0$ and $k_x=\pi/a$. The Zak phase θ_y for any value of k_x is quantized as π, and hence a semi-infinite system possesses a topological boundary mode which is located inside the band gap with dispersion connecting the two band edges [37]. (See appendix A) The FSE introduces coupling between two such boundary modes located at the $+y$ and $-y$ boundaries if the system is finite.

Then we proceed to investigate the FSE for a finite number of lattice sites (N_y) along the y-direction. First, we start with an extreme case where $N_y=1$. This case corresponds to an infinite chain of dipoles. In this case, P_x and P_y dipoles decouple and exhibit positive and negative dispersions, respectively [42]. These two bands cross once at $k_x=\pi/2a$. When $N_y=2$, *i.e.* two coupled infinite chains, P_x and P_y dipoles couple with each other and there is no pure band with only P_x or P_y component. Instead, one can label the band with either mirror symmetric (even) or antisymmetric (odd). As shown in figure 3(b), there are now four bands in total and two of them appear inside the bulk gap region, with one even state (red) and one odd state (blue) for the P_y component. Interestingly, now the red and blue bands cross with each other twice which is also the number of the coupled chains. As we further increase N_y as shown in figures 3(c) and (d), the red and blue bands approach the dispersion of the boundary modes for a semi-infinite system. Still, the number of nodes is always equal to N_y. Meanwhile, the gray bands start filling up the projection of the bulk periodic bands. These gray bands are hence bulk modes inside a finite system. Recently, chiral anomaly bulk states (CABSs) in finite systems have drawn intense interest [43–46]. These CABSs are originated from the nontrivial topology of the systems under consideration. In contrast, the bulk modes in our system are topologically trivial, and hence we only focus on the boundary modes in the following.

To prove that the number of nodes between the even and odd modes is equal to N_y, we analytically solve the system. (Proof in appendix B). We first obtain the eigen energy and eigenstates of the boundary mode for a semi-infinite system as

$$E_e = -\frac{\cos k_x \left[6\sqrt{2}\sin k_x + 3\cos k_x \sin k_x + \xi\left(\cos^2 k_x + 6\sqrt{2}\cos k_x + 16\right)\right]}{\xi\left(\sqrt{2}\cos k_x + 8\right) + 3\sqrt{2}\sin k_x}, \tag{11}$$

and

$$\boldsymbol{P}_e = \{p_1, p_2, \ldots, p_i, \ldots\}\begin{pmatrix} 1 \\ i\xi \end{pmatrix}, \tag{12}$$

respectively. In equation (12), the subscript labels the number of dipole chain, and the first (second) element inside the parenthesis represent the P_x (P_y) component.

$$\xi = \sqrt{\left(2\sqrt{2} - \cos k_x\right) / \left(4\sqrt{2} + \cos k_x\right)}, \tag{13}$$

and

$$p_n = \frac{1}{2^n N\sqrt{4d_1 + d_2^2}}\left[\left(d_2 + \sqrt{4d_1 + d_2^2}\right)^n - \left(d_2 - \sqrt{4d_1 + d_2^2}\right)^n\right], \tag{14}$$

with N being the normalization constant, $d_1 = -C_1/C_3$, $d_2 = -C_2/C_3$, and

$$\begin{cases} C_1 = \frac{1}{4}\left[\sqrt{2}\cos k_x + 3\sqrt{2}\xi\,\sin k_x - 4\right], \\ C_2 = 4\cos k_x - E_e, \\ C_3 = \frac{1}{4}\left[\sqrt{2}\cos k_x - 3\sqrt{2}\xi\,\sin k_x - 4\right]. \end{cases} \tag{15}$$

To solve for the FSE for the boundary modes in a finite system, we use the eigenfunction of the semi-infinite system as basis. Considering the finite system with N_y lattice sites, we truncate the wavefunction of the boundary mode of a semi-infinite system at the N_y site as $\{p_1, p_2, \ldots, p_{N_y}\}\left(\begin{smallmatrix} 1 \\ i\xi \end{smallmatrix}\right)$. Then the eigenstates of the finite system are constructed as superpositions of two truncated boundary modes ((see the equation (B5) of appendix B for details)). Such a truncation inevitably induces approximation. We assume that the perturbation introduced by this approximation is small, which also indicates that the energy splitting between the boundary modes is small. With perturbation theory to the first order, we obtain that the hopping strength between the two boundary modes localized on opposite boundaries is

$$\Delta E = \frac{C_3\left(p_1 p_{N_y - 1} - p_2 p_{N_y}\right)}{p_1\left(p_1 + p_{N_y}\right)}. \tag{16}$$

Thus, to the first-order approximation, the frequencies of the even and odd boundary modes are $E_e + \Delta E$ and $E_e - \Delta E$, respectively. When $\Delta E = 0$, the hopping strength is zero thus the FSE vanishes, and then there is a nodal point on the even and odd boundary bands. It can be proved that ΔE is an oscillation function of k_x and exhibits N_y zeros for $k_x \in (0, \pi/a)$. (Detail proof is also provided in appendix B). To check that the zeros of ΔE indeed predict the number of nodes, we provide the locations of boundary band nodes (red $+$) and the zeros of ΔE (blue square) in figure 3(e). The number of the red $+$ exactly equals the number of the blue square for every N_y, and the difference comes from the first-order approximation we take. With the increase of N_y where the prediction of ΔE works better, red $+$ and blue square approach each other.

3. Filtering effect

The peculiar FSE discussed here can also leads to potential applications. Different from traditional FSEs that need lots of lattice sites to suppress, here the FSE is absence for just a very few lattices sites which hence greatly reduces the size of the strip in wave guiding. In addition, the particular FSE occurs only at some isolated wavevectors, and this feature can help to select the target wave components [47]. For instance, the boundary modes can be utilized as waveguide channels to guide waves. In our system, the coupling strength between two boundary modes on opposite sides vanishes at these nodes and thus each boundary mode can

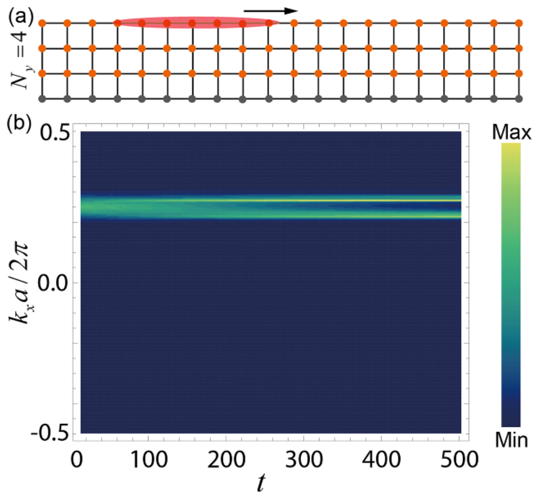

Figure 4. (a) Sketch of the system in simulation, which is long enough along the x-direction and 4 along the y-direction. Orange and gray represent lattice sites with no absorption and finite absorption $\gamma_1=-0.2i$, respectively. (b) The normalized amplitude of wave package in the momentum space as a function of the evolution time t.

be confined to one side of the waveguide as it propagates. As the coupling between boundary modes localized on two boundaries is a function of k_x and N_y, we can use this unique feature to filter out the component we need. In figure 4, we demonstrate this effect. The system consists of four chains ($N_y=4$) and the wave function is assumed to be initially only on the 4th chain as sketched in figure 4(a) with the amplitude given by

$$\psi_{m,4}(t=0)=\exp\left[ik_{x0}ma-\frac{(m-m_0)^2}{w^2}\right]\begin{pmatrix}1\\ i\xi(k_{x0})\end{pmatrix}, \tag{17}$$

where we assume a Gaussian package with center wave vector, width and center position given by $k_{x0}=\pi/2a$, $w=10$ and $m_0=20$, respectively. Such a Gaussian package's wave vector components cover the wave vectors of the middle two nodes for N_y=4. ξ is set as $\xi=0.71$ to match the boundary modes at k_{x0} as given by equation (13). All the lattice sites are set as lossless (orange) except the first column which is absorptive with onsite energy $\gamma_1=-0.2i$. We solve the time-dependent Schrodinger equation. For simplicity, we set $\hbar=1$ in the simulation. With the propagating of the wave package, the components whose wave vectors are not at nodes couple to opposite sides and get absorbed eventually since the 1st chain is absorptive. The components whose wave vectors are at nodes remain almost unchanged and localized on the original upper boundary. Figure 4(b) gives the normalized k_x component as a function of evolution time. At $t=0$, it exhibits a Gaussian shape centered at k_{x0} as given by equation (17). With the increase of t, the unwanted components get absorbed and the Gaussian shape gradually evolves to two sharp peaks at $k_xa/2\pi=0.22$ and 0.28, which are exactly the k_x values of nodes at which the two boundary modes decoupled.

4. Plasmonic sphere array with this FSE

Up to this point, we used a tight-binding model with next-nearest neighbor coupling to reveal the physics of such a peculiar FSE. We then demonstrate that such a novel effect exists with full wave simulations when all the coupling terms are considered. As our system only requires the symmetry imposed by the P_x and P_y modes in a square lattice, the FSE discussed herein should be quite universal. Possible candidates are photonic crystals, phononic crystals, cold atoms, and 2D materials with properly chosen orbitals. Below we show that this peculiar type of FSE also exists in a plasmonic sphere array consisting of plasmonic nanoparticles whose electronic wavefunction can couple to electromagnetic radiation with wavelengths much larger than the particle [48]. The interaction between electromagnetic waves and plasmonic nanoparticles in periodic plasmonic sphere arrays leads to lattice plasmon modes with hybrid photonic–plasmonic character [49]. We consider a square lattice array of plasmonic spheres with lattice constant $a=50\,\text{nm}$ and the radius of the sphere $r_S=20\,\text{nm}$. Similar plasmonic metal nanoparticle arrays have been fabricated using advanced micro and nano fabrication methods [50–52]. We employ a Drude model for the sphere: $\varepsilon(\omega)=1-\omega_p^2/\omega\left(\omega+i\gamma_p\right)$ with the plasmon frequency $\omega_p=4\,\text{eV}$ and the damping coefficient $\gamma_p=0.01\,\text{eV}$. The local electromagnetic field at the position of a dipole is composed of the external incident field and the field emitted by all other dipoles. At the location of the local dipole, the local field E_{local} induces a dipole moment P_i, which in turn acts as a source of radiation for the other dipoles. The response of this plasmonic sphere array to external electromagnetic waves can be obtained semi-analytically with the coupled-dipole equation [40, 53]:

$$\boldsymbol{p}_m = \alpha\left[\boldsymbol{E}_m^{\mathrm{ext}} + \sum\nolimits_{m\neq n} \overleftrightarrow{\boldsymbol{W}}\left(\boldsymbol{R}_m - \boldsymbol{R}_n\right)\boldsymbol{p}_n\right], \tag{18}$$

where $\mathbf{p}_m$ represents the dipole moment at location $\mathbf{R}_m$, $\mathbf{E}_m^{\mathrm{ext}}$ is the corresponding local external electric field, and $\alpha\left(\omega\right) = i3a_1\left(\omega\right)/2k_0^3$ is the dynamic dipole polarizability, where $k_0 = \omega/c$ is the wave vector in vacuum with c being the speed of light, $a_1\left(\omega\right)$ is the electric dipolar term of the Mie coefficients [54]. $\overleftrightarrow{\boldsymbol{W}}$ is the dyadic Green's function,

$$\overleftrightarrow{\boldsymbol{W}}\left(\boldsymbol{r}\right) = k_0^3\left[A\left(k_0 r\right)\boldsymbol{I}^{3\times3} + B\left(k_0 r\right)\frac{\boldsymbol{rr}}{r^2}\right], \tag{19}$$

with $\mathbf{I}^{3\times3}$ being the 3×3 identity matrix and

$$\begin{cases} A\left(k_0 r\right) = \left[\left(k_0 r\right)^{-1} + i\left(k_0 r\right)^{-2} - \left(k_0 r\right)^{-3}\right]e^{ik_0 r}, \\ B\left(k_0 r\right) = \left[-\left(k_0 r\right)^{-1} - 3i\left(k_0 r\right)^{-2} + 3\left(k_0 r\right)^{-3}\right]e^{ik_0 r}. \end{cases} \tag{20}$$

Note here, when the wavelength is much larger than the lattice constant, *i.e.* $k_0 r \ll 1$, $\left(k_0 r\right)^{-3}$ terms dominate in $A\left(k_0 r\right)$ and $B\left(k_0 r\right)$, and $e^{ik_0 r} \approx 1$. Thus we get the quasi-static limit [42, 55, 56] and $\overleftrightarrow{\boldsymbol{W}}$ reduces to the hopping in equation (6).

The equation (18) can be written as

$$\alpha^{-1}\boldsymbol{p}_m - \sum\nolimits_{m\neq n}\overleftrightarrow{\boldsymbol{W}}\left(\boldsymbol{R}_m - \boldsymbol{R}_n\right)\boldsymbol{p}_n = \boldsymbol{E}_m^{\mathrm{ext}}. \tag{21}$$

According to the Bloch's theorem for periodic systems, the periodic boundary conditions can be applied:

$$\boldsymbol{p}_m = \boldsymbol{p}e^{i\boldsymbol{k_B}\boldsymbol{R}_m}, \tag{22}$$

$$\boldsymbol{E}_m^{\mathrm{ext}} = E^{\mathrm{ext}}\boldsymbol{e}^{i\boldsymbol{k_B}\boldsymbol{R}_m}, \tag{23}$$

where $\boldsymbol{k_B}$ is the Bloch wave vector, and the external field (equation (23)) is chosen to excite an eigenmode associated with the Bloch vector selectively [57]. We put equations (22) and (23) into equation (21) and have $\boldsymbol{Mp} = \boldsymbol{E}^{\mathrm{ext}}$, where $\boldsymbol{E}^{\mathrm{ext}}$ is a vector whose components are the electric fields of the external incident wave, and $\boldsymbol{M}$ is a matrix operator on vector $\mathbf{p}$,

$$\boldsymbol{M} = \alpha^{-1} - \overleftrightarrow{\boldsymbol{G}}, \tag{24}$$

there $\overleftrightarrow{\boldsymbol{G}} = \sum_{\boldsymbol{R}'\neq\boldsymbol{R}_0}\overleftrightarrow{\boldsymbol{W}}\left(\boldsymbol{R}_0 - \boldsymbol{R}'\right)\boldsymbol{e}^{i\boldsymbol{k_B}\left(\boldsymbol{R}'-\boldsymbol{R}_0\right)}$ is the lattice sum of the dipolar Green's function, an infinite series capturing dipolar interactions from all lattice sites, extending beyond the scope of the tight-binding model. One can define the eigen polarizability as $\alpha_{\mathrm{eig}} = \lambda^{-1}$ with λ being the eigenvalue of $\mathbf{M}$ [40, 57]. In a periodic system, α_{eig} is a function of ω and the Bloch wave vector. The eigen polarizability α_{eig} is derived from the intrinsic polarizability of a plasmonic sphere, combined with the scattering influences from other spheres situated at periodic lattice sites. It captures the intrinsic properties of individual particles, along with the interparticle coupling determined by the lattice's geometric configuration. For a passive system, $\mathrm{Im}\left[\alpha_{\mathrm{eig}}\right]$ is always positive and exhibits a peak in the presence of a resonance, which outlines the band dispersion in scenarios of minimal dissipation. Moreover, $\mathrm{Im}\left[\alpha_{\mathrm{eig}}\right]$ is proportional to the extinction of the driving field, and the width of an extinction peak on ω is proportional to the mode quality [40, 57]. Hence the summation of all the imaginary parts of the eigen-polarizabilities, *i.e.* $\mathrm{Im}\left[\sum\alpha_{\mathrm{eig}}\right]$ can represent the resonance response of the system. Considering the strip geometry with a finite width, the dispersion of plasmonic sphere arrays presents similar node characteristics. In figure 5, we set $N_y = 3$ and show $\mathrm{Im}\left[r_S^{-3}\sum\alpha_{\mathrm{eig}}\right]$ as a function of k_x and energy. The resonance peak shows the dispersion of such a plasmonic sphere array. In addition to the dispersion, this plot automatically shows the presence of light cone (marked by the black dashed line in figure 5) as the interaction of the plasmonic spheres with the free propagating wave is taken into consideration. Except for that, the dispersion is quite similar to figure 3(c). Here we can also find three nodes (marked by the red dots) between the middle two bands. Hence we have numerically demonstrated the fact that the nodes of FSE are not limited to the tight-binding Hamiltonian in equation (10). The underlying physics should be universal even in the presence of the light cone when we consider P_x and P_y orbitals in a square lattice.

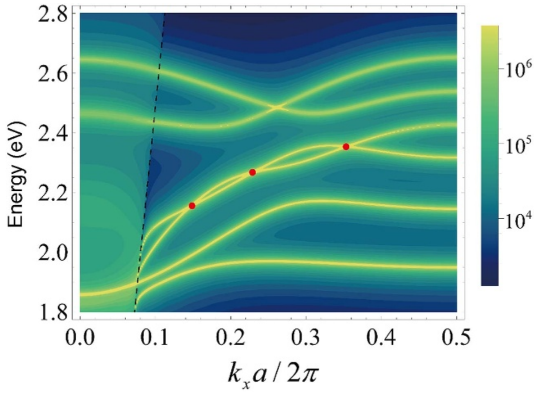

Figure 5. Im[$r_S^{-3}\sum\alpha_{\text{eig}}$] as a function of k_x and the energy of the electromagnetic waves. Here the black dashed line marks the position of the light cone, and the red dots highlight the positions of nodes on the boundary modes. In this plot, the lattice constant is $a = 50\,\text{nm}$, the radius of the plasmonic sphere is $r_S = 20\,\text{nm}$, the plasmonic frequency is $\omega_p = 4\,\text{eV}$ and the damping coefficient is $\gamma_p = 0.01\,\text{eV}$.

5. Summary

In summary, we analytically solved a next-nearest-neighbor hopping model to investigate the FSE of boundary modes. The boundary modes of a finite-width strip twist around each other, intersecting at nodes and the number of nodes equals the number of lattice sites across the strip. This FSE leads to a special type of filtering effect where only the components with wave vectors that match those of the nodes are preserved. Meanwhile, this peculiar FSE is general and also presents in the plasmonic sphere array. Our model is based on just in-plane dipole orbitals and needs no further assumption, and the FSE discussed here can be found in electronic waves, classical waves and cold atoms. Our work points to the possibility of getting rid of the formation of gaps due to FSE with properly chosen orbitals and lattice, and thus opens a feasible way for integrating multiple waveguides into a compact device.

Data availability statement

All data that support the findings of this study are included within the article (and any supplementary files).

Acknowledgments

We thank Zhao-Qing Zhang and Ruo-Yang Zhang for helpful discussions. This work is supported by the National Natural Science Foundation of China—Research Grants Council of Hong Kong (NSFC-RGC) Joint Research Scheme (Grant No. 12321161645), and National Natural Science Foundation of China (Grant Nos. 12274332, 12274330 and 12334015). C T C is supported by Research Grants Council (RGC) Hong Kong through Grants CRS_HKUST601/23 and AoE/P-502/20. Y L is supported by the National Natural Science Foundation of China (Grant Nos. 12174188 and 11974176). D W is also supported by the Knowledge Innovation Program of Wuhan-Shuguang (Grant No. 2022010801020125) and the 'Xiaomi Young Scholar Program' at Wuhan University.

Appendix A. Band structure of the periodic system and boundary modes dispersion

In this section, we provide the band structure of the periodic tight-binding system and the dispersion of the boundary mode for a semi-infinite system. Figure 6(a) gives the band structure of the periodic system. For the dispersion of the boundary mode, we use a finite system with a large enough N_y. When N_y is large enough, the coupling between the two boundary modes on opposite sides becomes extremely small, as can be seen in figure 6(b) with $N_y = 20$. The red (even mode) and blue curves (odd mode) almost overlap with each other. The dispersion of the boundary mode for a semi-infinite system can then be obtained by taking the average of these two curves [37].

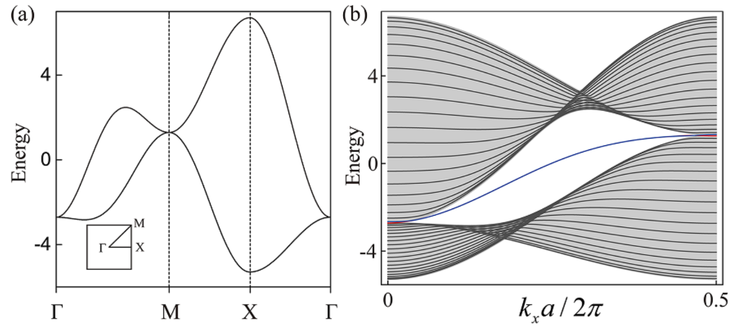

Figure 6. (a) The band structure of the periodic tight-binding model. (b) Band dispersion with $N_y = 20$, where the gray background represents the projection of the periodic bulk band. The Hamiltonian is provided in equation (10) of the main text.

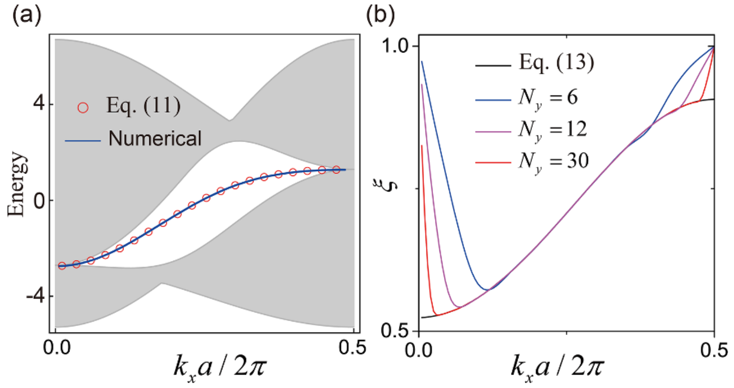

Figure 7. (a) The boundary mode dispersions obtained from equation (11) (open red circle) and the numerical simulations (blue line). Here the gray regions represent the projection of the bulk bands. (b) Comparing of ξ obtained from equation (13) for a semi-infinite system and the numerically obtained value for different N_ys.

Appendix B. The proof that the number of nodes equals toN_y

In this section, we analytically prove that the number of nodes equals N_y. We first obtain the dispersion and the wave function of the boundary modes for a semi-infinite system. This boundary mode satisfies the equation

$$H_{\text{semi}}\left(k_x\right)\mathbf{P}_e\left(k_x\right) = E_e\left(k_x\right)\mathbf{P}_e\left(k_x\right), \tag{B1}$$

where H_{semi} is the Hamiltonian of a semi-infinite system and E_e is the eigen energy. The boundary mode wave function of a semi-infinite system is provided in equation (12). After some simple math, we obtain the eigen energy (equation (11)) and the ξ (equation (13)). Meanwhile, the series $\{p_1, p_2, \ldots, p_i, \ldots\}$ satisfies the condition

$$\begin{cases} C_1 p_{i-1} + C_2 p_i + C_3 p_{i+1} = 0, \\ C_2 p_1 + C_3 p_2 = 0, \end{cases} \tag{B2}$$

with p_1 being used for normalization and equation (B2) provides a recurrence relation for p_n. The specific form of p_n is presented in equation (14), and C_1, C_2 and C_3 are given in equation (15). As a preliminary check, we compare equations (11) and (13) with numerical results from finite systems as shown in figures 7(a) and (b), respectively. Figure 7(a) shows the comparison of numerically obtained boundary mode dispersion for a large enough system (blue line) and that from equation (11) (open red disk). They agree with each other perfectly well. In figure 7(b), the black line is obtained from equation (13), and the blue, magenta and red represent $\left|p_{1y}/p_{1x}\right|$ for $N_y = 6,\ 12,\ 30$, respectively. It is clear that with the increasing of N_y, numerical results approaching that from equation (13). Meanwhile, numerical results deviate from equation (13) near $k_x = 0$ and π/a whereat the band gaps close.

The coefficient 2^{-n} in equation (14) provides the exponentially decaying feature of p_n with the increasing of n. To obtain more detailed features of p_n, we need the information of d_2 and $\sqrt{4d_1 + d_2^2}$ as functions of k_x,

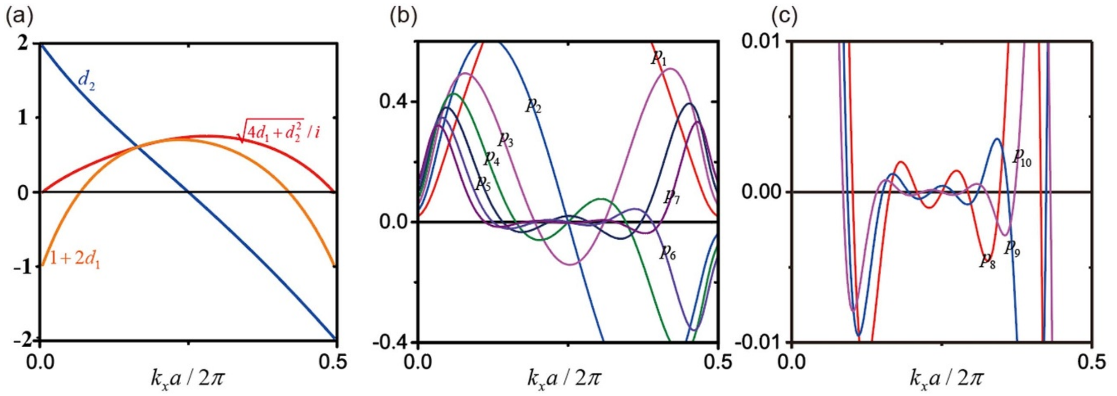

Figure 8. (a) $\sqrt{4d_1+d_2^2}/i$ (red), d_2 (blue), $1+2d_1$ (orange) as a function of k_x. (b), (c) p_n as functions of k_x, where different colors for different n. p_n is an oscillation function of k_x and has $n-1$ zeros.

which are provided in figure 8(a). It can be shown that d_2 is a monotonically decreasing function of k_x, and $\sqrt{4d_1+d_2^2}$ is purely imaginary and exhibits a $\sin k_x$-like shape. We can define

$$\theta=\arg\left(d_2+\sqrt{4d_1+d_2^2}\right), \tag{B3}$$

and show that θ is a monotonically increasing function of k_x. $\theta=0$ when $k_x=0$; $\theta=\pi$ when $k_xa=\pi$. Taking equation (B3) into equation (14), we have

$$p_n=\frac{(-2d_1)^{n-1}}{N}\frac{\sin(n\theta)}{\sin\theta}. \tag{B4}$$

We can see that $\{p_1,p_2,\ldots,p_i,\ldots\}$ are oscillating decaying functions of the chain index i. Noting that θ is a monotonically increasing function of k_x, p_n should thus also be an oscillation function of k_x, which gives the essential reason for the emergence of nodes. And equation (B4) proves that p_n possesses $n-1$ zeros for $k_x\in(0,\pi)$. The first few p_n functions are provided in figures 8(b) and (c). We can clearly see the oscillation feature and observe that p_n exhibits $n-1$ zeros.

For a finite system with N_y, the wave function of the boundary mode should be

$$\boldsymbol{P}_{\text{finite}}=\left(\{p_1,p_2,\ldots,p_{N_y-1},p_{N_y}\}\pm\{p_{N_y},p_{N_y-1},\ldots,p_2,p_1\}\right)\begin{pmatrix}1\\ i\xi\end{pmatrix}. \tag{B5}$$

The wave function satisfies

$$\begin{pmatrix}\tilde{C}_2 & C_3 & & & \\ C_1 & \tilde{C}_2 & C_3 & & \\ & \ddots & \ddots & \ddots & \\ & & C_1 & \tilde{C}_2 & C_3\\ & & & C_1 & \tilde{C}_2\end{pmatrix}\begin{pmatrix}p_1\pm p_{N_y}\\ p_2\pm p_{N_y-1}\\ \vdots\\ p_{N_y-1}\pm p_2\\ p_{N_y}\pm p_1\end{pmatrix}=0, \tag{B6}$$

where $\tilde{C}_2=4\cos k_x+E_e\pm\Delta E$ with ΔE being half of the energy difference between the even and odd modes. ΔE also equals the hopping strength between the boundary modes localized on different boundaries. If we assume that ΔE is a small number and can thus treat it as a perturbation. Then to the first order of ΔE, the formula was provided as equation (16).

Considering the fact that $C_3/p_1\left(p_1+p_{N_y}\right)$ exhibit no zeros, and combined with equation (14), we find that the zeros of ΔE is the same as the function (the numerator without some trivial constants)

$$\begin{aligned}\Delta\tilde{E}_n&=(1+2d_1)\,d_2\left[\left(d_2+\sqrt{4d_1+d_2^2}\right)^n-\left(d_2-\sqrt{4d_1+d_2^2}\right)^n\right]\\&\quad+\sqrt{4d_1+d_2^2}\left[\left(d_2+\sqrt{4d_1+d_2^2}\right)^n+\left(d_2-\sqrt{4d_1+d_2^2}\right)^n\right]\\&=i(-4d_1)^{n+1}\left[-(1+2d_1)\cos\theta\sin(n\theta)+\sin\theta\cos(n\theta)\right],\end{aligned} \tag{B7}$$

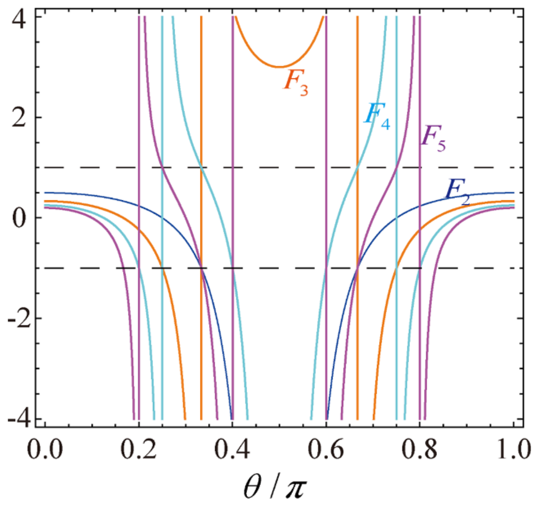

Figure 9. F_i defined in equation (B8*a*) with $i \in \{2,\ 3,\ 4,\ 5\}$ as a function of θ. The black dashed lines are $y = 1$ and $y = -1$ for reference.

where n represents the dimension of the truncated wave function, i.e., N_y. And equation (B3) is used in the last step. Noting that $d_1 < 0$ (see figure 8(a)), the zeros of $\Delta\tilde{E}_n$ are the solutions of the following equations,

$$1 + 2d_1 = F_n \equiv \tan\theta \cot(n\theta), \tag{B8a}$$

or

$$\sin(n\theta) = \sin\theta = 0. \tag{B8b}$$

Equation (B8*b*) is satisfied when n is an odd number and $k_x a = \pi/2$. For equation (B8*a*), we first notice that F_n exhibits the following features as shown in figure 9:

a. F_n is a monotonic decreasing function of θ for $\theta < \pi/2$ and a monotonic increasing function of θ for $\theta > \pi/2$.
b. F_n exhibits $n-1$ singular points at $\theta = m\pi/n$, where $m \in \{1, 2, \ldots, n-1\}$. Meanwhile F_n diverges when θ approaching these singular points.

Taking the value of $1 + 2d_1$ as given in figure 8(a) into consideration, we can conclude that there are in total n zeros for $\Delta\tilde{E}_n$ as a function of k_x for $k_x a \in (0, \pi)$.

ORCID iDs

Tao Liu https://orcid.org/0000-0001-7947-2761
Duanduan Wan https://orcid.org/0000-0002-9429-7735
Yun Lai https://orcid.org/0000-0002-0040-9274
C T Chan https://orcid.org/0000-0002-9335-8110
Meng Xiao https://orcid.org/0000-0002-2087-3007

References

[1] Ashoori R 1996 Electrons in artificial atoms *Nature* **379** 413–9
[2] Banin U, Cao Y, Katz D and Millo O 1999 Identification of atomic-like electronic states in indium arsenide nanocrystal quantum dots *Nature* **400** 542–4
[3] Kittel C 2004 *Introduction to Solid State Physics* (Wiley)
[4] Joannopoulos J D, Johnson S G, Winn J N and Meade R D 2008 *Photonic Crystals: Molding the Flow of Light* 2nd edn (Princeton University Press)
[5] O'brien J L, Furusawa A and Vučković J 2009 Photonic quantum technologies *Nat. Photon.* **3** 687–95
[6] Saffman M, Walker T G and Mølmer K 2010 Quantum information with Rydberg atoms *Rev. Mod. Phys.* **82** 2313
[7] Imamog¯lu A, Awschalom D D, Burkard G, Di Vincenzo D P, Loss D, Sherwin M and Small A 1999 Quantum information processing using quantum dot spins and cavity QED *Phys. Rev. Lett.* **83** 4204–7
[8] Cirac J I, Zoller P, Kimble H J and Mabuchi H 1997 Quantum state transfer and entanglement distribution among distant nodes in a quantum network *Phys. Rev. Lett.* **78** 3221

[9] Pellizzari T, Gardiner S A, Cirac J I and Zoller P 1995 Decoherence, continuous observation, and quantum computing: a cavity QED model *Phys. Rev. Lett.* **75** 3788
[10] Horodecki R, Horodecki P, Horodecki M and Horodecki K 2009 Quantum entanglement *Rev. Mod. Phys.* **81** 865
[11] Akopian N, Lindner N H, Poem E, Berlatzky Y, Avron J, Gershoni D, Gerardot B D and Petroff P M 2006 Entangled photon pairs from semiconductor quantum dots *Phys. Rev. Lett.* **96** 130501
[12] Aspuru-Guzik A and Walther P 2012 Photonic quantum simulators *Nat. Phys.* **8** 285–91
[13] Zhang X-L, Yu F, Chen Z-G, Tian Z-N, Chen Q-D, Sun H-B and Ma G 2022 Non-Abelian braiding on photonic chips *Nat. Photon.* **16** 390–5
[14] Arrazola J M *et al* 2021 Quantum circuits with many photons on a programmable nanophotonic chip *Nature* **591** 54–60
[15] Haus H A and Šipilov K F 1984 *Waves and Fields in Optoelectronics* (Prentice-Hall)
[16] Song T, Chu H, Luo J, Cao Z, Xiao M, Peng R, Wang M and Lai Y 2022 Ultracompact photonic circuits without cladding layers *Phys. Rev.* X **12** 011053
[17] Hasan M Z and Kane C L 2010 Colloquium: topological insulators *Rev. Mod. Phys.* **82** 3045
[18] Qi X-L and Zhang S-C 2011 Topological insulators and superconductors *Rev. Mod. Phys.* **83** 1057
[19] Ozawa T *et al* 2019 Topological photonics *Rev. Mod. Phys.* **91** 015006
[20] Ma G, Xiao M and Chan C T 2019 Topological phases in acoustic and mechanical systems *Nat. Rev. Phys.* **1** 281–94
[21] Haldane F D M and Raghu S 2008 Possible realization of directional optical waveguides in photonic crystals with broken time-reversal symmetry *Phys. Rev. Lett.* **100** 013904
[22] Wang Z, Chong Y D, Joannopoulos J D and Soljačić M 2008 Reflection-free one-way edge modes in a gyromagnetic photonic crystal *Phys. Rev. Lett.* **100** 013905
[23] Wang Z, Chong Y, Joannopoulos J D and Soljačić M 2009 Observation of unidirectional backscattering-immune topological electromagnetic states *Nature* **461** 772–5
[24] Yu Z, Veronis G, Wang Z and Fan S 2008 One-way electromagnetic waveguide formed at the interface between a plasmonic metal under a static magnetic field and a photonic crystal *Phys. Rev. Lett.* **100** 023902
[25] Ni X, Li M, Weiner M, Alù A and Khanikaev A B 2020 Demonstration of a quantized acoustic octupole topological insulator *Nat. Commun.* **11** 1–7
[26] Hu M, Zhang Y, Jiang X, Qiao T, Wang Q, Zhu S, Xiao M and Liu H 2021 Double-bowl state in photonic Dirac nodal line semimetal *Light Sci. Appl.* **10** 170
[27] Zhou B, Lu H-Z, Chu R-L, Shen S-Q and Niu Q 2008 Finite size effects on helical edge states in a quantum spin-Hall system *Phys. Rev. Lett.* **101** 246807
[28] Ezawa M and Nagaosa N 2013 Interference of topologically protected edge states in silicene nanoribbons *Phys. Rev.* B **88** 121401
[29] Linder J, Yokoyama T and Sudbø A 2009 Anomalous finite size effects on surface states in the topological insulator $\mathrm{Bi_2Se_3}$ *Phys. Rev.* B **80** 205401
[30] Lu H-Z, Shan W-Y, Yao W, Niu Q and Shen S-Q 2010 Massive Dirac fermions and spin physics in an ultrathin film of topological insulator *Phys. Rev.* B **81** 115407
[31] Krueckl V and Richter K 2011 Switching spin and charge between edge states in topological insulator constrictions *Phys. Rev. Lett.* **107** 086803
[32] Zhang L, Cheng F, Zhai F and Chang K 2011 Electrical switching of the edge channel transport in HgTe quantum wells with an inverted band structure *Phys. Rev.* B **83** 081402
[33] Shockley W 1939 On the surface states associated with a periodic potential *Phys. Rev.* **56** 317
[34] Tamm I 1932 On the possible bound states of electrons on a crystal surface *Phys. Z Sowjetunion* **1** 733
[35] Liu C-X, Zhang H, Yan B, Qi X-L, Frauenheim T, Dai X, Fang Z and Zhang S-C 2010 Oscillatory crossover from two-dimensional to three-dimensional topological insulators *Phys. Rev.* B **81** 041307
[36] Liu F and Wakabayashi K 2017 Novel topological phase with a zero berry curvature *Phys. Rev. Lett.* **118** 076803
[37] Huang X, Xiao M, Zhang Z-Q and Chan C T 2014 Sufficient condition for the existence of interface states in some two-dimensional photonic crystals *Phys. Rev.* B **90** 075423
[38] Purcell E M and Pennypacker C R 1973 Scattering and absorption of light by nonspherical dielectric grains *Astrophys. J.* **186** 705–14
[39] Markel V 1993 Coupled-dipole approach to scattering of light from a one-dimensional periodic dipole structure *J. Mod. Opt.* **40** 2281–91
[40] Fung K H and Chan C T 2007 Plasmonic modes in periodic metal nanoparticle chains: a direct dynamic eigenmode analysis *Opt. Lett.* **32** 973–5
[41] Jackson J D 1998 *Classical Electrodynamics Third Edition* (Wiley)
[42] Brongersma M L, Hartman J W and Atwater H A 2000 Electromagnetic energy transfer and switching in nanoparticle chain arrays below the diffraction limit *Phys. Rev.* B **62** R16356
[43] Jia H, Zhang R, Gao W, Guo Q, Yang B, Hu J, Bi Y, Xiang Y, Liu C and Zhang S 2019 Observation of chiral zero mode in inhomogeneous three-dimensional Weyl metamaterials *Science* **363** 148–51
[44] Peri V, Serra-Garcia M, Ilan R and Huber S D 2019 Axial-field-induced chiral channels in an acoustic Weyl system *Nat. Phys.* **15** 357–61
[45] Wang M, Ma Q, Liu S, Zhang R-Y, Zhang L, Ke M, Liu Z and Chan C 2022 Observation of boundary induced chiral anomaly bulk states and their transport properties *Nat. Commun.* **13** 5916
[46] Xia H-R and Xiao M 2023 Reversal of the chiral anomaly bulk states with periodically staggered potential *Phys. Rev.* B **107** 035144
[47] Liu T, Bai K, Zhang Y, Wan D, Lai Y, Chan C and Xiao M 2023 Finite barrier bound state *Light Sci. Appl.* accepted
[48] Novotny L and Hecht B 2012 *Principles of Nano-Optics* (Cambridge University Press)
[49] Ross M B, Mirkin C A and Schatz G C 2016 Optical properties of one-, two-, and three-dimensional arrays of plasmonic nanostructures *J. Phys. Chem.* C **120** 816–30
[50] Henzie J, Lee M H and Odom T W 2007 Multiscale patterning of plasmonic metamaterials *Nat. Nanotechnol.* **2** 549–54
[51] Zhou W, Dridi M, Suh J Y, Kim C H, Co D T, Wasielewski M R, Schatz G C and Odom T W 2013 Lasing action in strongly coupled plasmonic nanocavity arrays *Nat. Nanotechnol.* **8** 506–11
[52] Yang A, Hoang T B, Dridi M, Deeb C, Mikkelsen M H, Schatz G C and Odom T W 2015 Real-time tunable lasing from plasmonic nanocavity arrays *Nat. Commun.* **6** 6939

[53] Weber W and Ford G 2004 Propagation of optical excitations by dipolar interactions in metal nanoparticle chains *Phys. Rev.* B **70** 125429

[54] Bohren C F and Huffman D R 1998 *Absorption and Scattering of Light by Small Particles* (Wiley Science Paperback Series) (Wiley-VCH)

[55] Han D, Lai Y, Zi J, Zhang Z-Q and Chan C T 2009 Dirac spectra and edge states in honeycomb plasmonic lattices *Phys. Rev. Lett.* **102** 123904

[56] Wang L, Zhang R-Y, Xiao M, Han D, Chan C T and Wen W 2016 The existence of topological edge states in honeycomb plasmonic lattices *New J. Phys.* **18** 103029

[57] Zhen Y-R, Fung K H and Chan C T 2008 Collective plasmonic modes in two-dimensional periodic arrays of metal nanoparticles *Phys. Rev.* B **78** 035419